Toward high energy density cathode materials for sodium-ion batteries: investigating the beneficial effect of Aluminum doping on the P2-type structure

Ivana Hasa [a,b], Stefano Passerini [a,b,*] and Jusef Hassoun [c,*]

[a] Helmholtz Institute Ulm, Helmholtzstraße 11, 89081 Ulm, Germany.

[b] Karlsruhe Institute of Technology (KIT), PO Box 3640, 76021 Karlsruhe, Germany.

[c] Department of Chemical and Pharmaceutical Sciences, University of Ferrara, Via Fossato di Mortara, 44121, Ferrara, Italy

*stefano.passerini@kit.edu, jusef.hassoun@unife.it

Keywords

Sodium-ion battery; P2-layered oxide cathode; aluminum doping.

Abstract

Aluminum doping of P2-type layered structure results in a Na-ion cathode material ($Na_{0.6}Ni_{0.22}Al_{0.11}Mn_{0.66}O_2$) with excellent performance. The material, in fact, exhibits outstanding specific capacities, 250 mAh g^{-1} and 150 mAh g^{-1} at 0.1 and 5C rate, respectively, which have never been reported before. Herein, a deep investigation on both the electrochemical behavior and the structural and morphological properties upon cycling reveals the beneficial effect of Aluminum and the importance of a proper metal intermixing selection for the obtainment of high performance cathode materials.

1. Introduction

Since 1980s, alkali-based rechargeable batteries, such as lithium-ion batteries (LIBs) and sodium-ion batteries (SIBs) represented the most appealing electrochemical energy storage systems due to their reversibility and high-energy content. So far, the higher electrochemical performances of LIBs, mostly in terms of energy density, vanished the interest on SIBs. However, the recent growth of the energy storage market renewed the interest on new systems characterized by low cost and environmental

sustainability.[1–3] Early estimations predicted a cost reduction of about 30% by the development of the Na-ion technology with respect to the lithium-based one, principally due to the limited economic impact of the sodium based raw materials, including the electrolyte solution and the possible use of aluminum as current collector instead of copper at the negative electrode.[4] The increasing number of recent scientific publications focused on new materials for application in sodium-ion battery, suggested this system as an appealing candidate for important fields such as large-scale stationary energy storage, in particular from renewable sources, in which the economic impact of the battery plays a key role.[5] The cathode materials proposed for SIBs principally belong to three classes of compounds, i.e., layered oxides, polyanionic frameworks and Prussian Blue Analogues (PBAs).[5–9] PBAs, such as $Na_xFeMn(CN)_6$, have been proposed as promising electrodes due to their low expected cost and favorable large alkali-ion channel with low activation barriers, however with issues associated to the role of hydration degree and interstitial H_2O.[9–12] Polyanion-based compounds have received larger attention since they can provide several advantages such as a high thermal and structural stability due to the strong covalent bonding of oxygen atoms, thus leading to safe and long-life cathode materials.[13] However, this class of compounds often suffers by poor electronic conductivity that is generally addressed by carbon coating process.[14] Layered oxides, basically stacking $(MO_2)_n$ sheets of MO_6 edge-sharing octahedral units,[15] reveal higher specific capacity and improved electrochemical performance at high currents with respect to polyanionic, compounds due to lower molecular weight and faster sodium diffusion, respectively.[16] The polymorphism character of this class of compounds is mainly driven by the orientation of the MO_6 octahedra along the c-axis direction leading to the formation of $(MO_2)_n$ layers along which alkali ions can be reversibly intercalated. In the specific case of sodium ions, taking into account its propensity to hexa-coordination, two different kind of sites are available, i.e. prismatic (P) or octahedral (O) ones.[15] The most common deriving structures for sodium-based layered transition metal oxides are indeed O3-, P2-, and P3-type, where the number indicates the transition metal layers in the repeating unit cell. It has

been widely reported that the P-type materials offer better electrochemical performances in sodium battery with respect to the corresponding O3-type structures, and among the P-type materials P2-structures have shown superior behavior with respect to P3- ones.[17–20] However, the cycling stability and energy density of P2-type layered oxides in sodium cells may be negatively affected by multiple phase transitions leading to structural instability of the host structure, reduction of the reversibility degree of the sodium (de-)insertion process and voltage decay upon cycling. The multiple phase transitions, through which P2-type materials undergo during the charge-discharge process, may be ascribed to the formation of ordered superstructures reflecting in distinct voltage plateaus upon the electrochemical cycling tests. It is reported that this kind of superstructures are mainly driven by the presence of charge ordering effects, which occur among the transition metals within a layer and Na^+/vacancy ordering attributable to the Na^+-Na^+ within the alkali metal layers. [21–25]

Among the P2-type materials, Na_xMnO_2 represents an attractive electrode due to the low cost, environmental compatibility and high specific capacity value. However, P2-type Mn-based oxides generally undergo several phase transitions during cell operation due to the Jahn-Teller deformation induced by Mn^{3+} and show a relatively low operating voltage basing on the redox couple Mn^{3+}/Mn^{4+}.[26,27] The main approach adopted to increase the operating voltage and improve the structural stability of P2-type Na_xMnO_2 has been focused on partial substitution of manganese by various metals, such as magnesium,[22] nickel [28,29] and iron. [17,30] Iron substituted P2-$Na_xMn_{0.5}Fe_{0.5}O_2$ has revealed interesting electrochemical properties in sodium cells due to the contribution of $Fe^{3+/4+}$ redox couple, however the air sensitivity and the capacity fading upon cycling represent two major issues to be addressed for the improvement of electrochemical performances. [17,30] In previous studies, it has been reported that, nickel incorporation in the layered oxide structure remarkably increases the average working potential, due to Ni^{2+}/Ni^{4+} couple, improves the capacity retention and enhances the energy efficiency of the overall electrochemical process in sodium cell. [19,20,23] The Na_xMO_2 (M=Ni, Fe, Mn) system revealed promising

performances, however, the iron incorporation effect and its role in the structural reorganization occurring at high voltage values during the de-sodiation process is still to be clarified and under investigation.[20,21,23] In view of the optimization of the electrochemical performance in terms of cycling stability and energy density, several metal intermixing strategies have been proposed.

Y. Li *et al.* recently proposed the air-stable P2-$Na_{7/9}Cu_{2/9}Fe_{1/9}Mn_{2/3}O_2$ exhibiting the Cu^{2+}/Cu^{3+} redox activity with excellent cyclability at 1C over 150 cycles, but delivering slightly less than 60 mAh g^{-1}. [31] However, the specific capacity at very low rates is comparable with that of P2-$Na_{2/3}Ni_{1/3}Mn_{2/3}O_2$. In order to improve the structural stability and increase the specific capacity of Ni-Mn based electrodes, substitution with Mg, Ti and Zn has been proposed as alternative high capacity materials. G. Singh *et al.*[32] proposed a $Na_{0.67}Mg_{0.1}Ni_{0.2}Mn_{0.7}O_2$ delivering 130 mAh g^{-1} within the 2.0-4.5 V voltage range. $Na_{2/3}Ni_{1/3}Mn_{1/2}Ti_{1/6}O_2$, proposed by H. Yoshida *et al.*,[33] delivers the same specific capacity in the same voltage window, while doping of the Ni-Mn based system with Zn enables the achievement of almost 140 mAh g^{-1} with about 85% capacity retention after 30 cycles at 12 mAg^{-1} in the 2.0-4.4 V voltage range.

Herein, we extended the study to a P2-type sodium layered oxide including nickel, manganese as well as light, low cost and electrochemically inactive aluminum. In this material, the electrochemically active Mn and Ni ensure high theoretical capacity exceeding 200 mA g^{-1} and operating voltage in sodium battery. The results reported in this work evidence that aluminum plays an important role in improving the material performance as electrode in sodium batteries both in terms of delivered capacity and cycling stability (Table S1).

2. Experimental

2.1 Material preparation

P2-type layered compound with nominal composition $Na_{0.6}Ni_{0.22}Al_{0.11}Mn_{0.66}O_2$ (NAM) was prepared by co-precipitation method dissolving stoichiometric proportions of $Ni(NO_3)_2 \cdot 6H_2O$ (Aldrich, trace metals basis 99,997%), $Al(NO_3)_4 \cdot 9H_2O$ (Aldrich, trace metals basis 99,997%) and $Mn(NO_3)_2 \cdot 4H_2O$ (Sigma Aldrich, purum p.a., ≥97.0%) in water and adding drop-wise an aqueous solution of NaOH (50% excess).The hydroxide precursor, was then filtrated, washed and dried overnight. Subsequently a solid state reaction among the nickel-aluminum-manganese precursor and NaOH in a molar ratio of 1:0.685 was performed in air atmosphere at 500°C for 5 hours. A final annealing step at 1000°C for 6 hours was then conducted for the pelletized material under air atmosphere and slowly cooled to room temperature.[20]

2.2 Material characterization

The sodium content and the transition metal ratio were determined by Inductively Coupled Plasma optical emission spectrometry (ARCOS ICP-OES, Spectro Analytical Instruments, Kleve, Germany). The structure of the sample was detected by X-Ray Diffraction (XRD) using the CuK_α radiation on the Bruker D8 Advance (Germany) diffractometer in the 2θ range from 10° to 90° with a step size of 0.01°. Rietveld refinement was performed by using TOPAS software with satisfactory agreement factor (R_{wp}=11.28%, GOF=1.22). The lattice parameter values were refined in the hexagonal *P6₃/mmc* space group using a pseudo-Voigt profile. The occupancy values were refined for Na(1) and Na(2) respectively in the *2b* and *2d* sites along with the isotropic atomic displacement parameters. The occupancy value for Mn, Ni and Al in the *2a* sites were also refined along with the positional coordinates for oxygen. The B_{iso} of Mn, Ni and Al were fixed to the same values. Ex-situ XRD was performed on pre-cycled electrodes, which were previously washed with anhydrous dimethyl carbonate (DMC) in order to remove electrolyte residuals inside an argon-filled glove box. The particle and electrode morphology were evaluated by using a high-resolution scanning electron microscope (FE-SEM, Zeiss Auriga) equipped by field emission electron gun as electron source and an in-lens detector. The acceleration voltage was set up to 3 kV. Qualitative elemental analysis was performed by energy dispersive X-ray spectroscopy (EDX).

2.3 Electrochemical characterization

The $Na_{0.6}Ni_{0.22}Al_{0.11}Mn_{0.66}O_2$ electrodes were prepared by dispersing the active material (85% w/w), carbon black super C electron conductor (Imerys, 10% w/w) and polyvinyldene fluoride binder (PVdF Kynar Flex 761A, Arkema Group, 10% w/w) in N-methyl-2-pyrrolidone (NMP, Aldrich). After intimate mixing and stirring, the slurry was casted on Al foil by doctor-blade technique, dried at 80°C overnight, punched as 12 mm-diameter electrodes, pressed and dried at 120°C under vacuum for 24 hours in order to remove residual traces of solvent and moisture. Finally, the electrodes were stored in an argon-filled glove box with a H_2O and O_2 content lower than 1 ppm. Swagelok® T-type sodium half-cells were assembled using 1M $NaPF_6$ (99+%, Alfa Aesar) in Propylene Carbonate (PC, UBE, Japan) as electrolyte solution soaked in a glass fiber (Whatmann GF/D) separator. Sodium metal was cut from sodium pieces (99.8%, Across Organics), roll pressed and finally punched on the current collector and used as counter and reference electrode. Cyclic voltammetry (CV) test was performed at a scan rate of 0.1mV sec^{-1} within the 4.6V-1.5V vs Na/Na^+ potential range with a multi-channel potentiostat-galvanostat (VMP3, Biologic Science Instruments). The $Na/Na_{0.6}Ni_{0.22}Al_{0.11}Mn_{0.66}O_2$ cells were cycled galvanostatically at 20 mA g^{-1} (the nominal capacity is 160mAh g^{-1}, corresponding to 0.6 equivalent of Na per mole of material) within various cut off voltages using a Maccor series 4000 battery tester (U.S.A). All the potential values are referred to the Na/Na^+ reference electrode. Electrochemical Impedance Spectroscopy (EIS) was performed using a multi-channel potentiostat-galvanostat (VMP3, Biologic Science Instruments) at various state of charge on a three electrodes cell applying a 10mV AC signal amplitude in the 200 kHz-10 mHz frequency range. Prior to each impedance measurement the cell voltage was hold until a current value of 1/100 was reached with respect to the initial current used for cycling. The obtained impedance spectra were fitted and analyzed using the Boukamp software (fitting error lower than 5%). All electrochemical measurements were performed in climatic chambers (KBF115, Binder GmbH) at 20°C ± 2 °C.

3. Results and discussion

The structural characteristics of layered $Na_{0.6}Ni_{0.22}Al_{0.11}Mn_{0.66}O_2$ (NAM) has been determined by X-ray diffraction analysis (Fig. 1). The material, belonging to the P2- type structure displayed in Fig. 1 inset, crystallizes without impurities within the hexagonal *P6₃/mmc* space group by ABBA arrangements of $(MO_2)_n$ sheets. Among these sheets, Na^+ ions occupy two different sites sharing faces (Na1) or edges (Na2) with the MO_6 octahedrons of adjacent layers. The Rietveld refinement of the XRD pattern reported in Fig. 1 allows the determination of the cell parameters and atomic occupancies reported in Tab. 1. The refined cell parameters, *i.e.* a = 2.8737(1) Å (related to the M-M intra-layer distance) and c =11.203(6) Å (related to the inter-layer distance), are very close to those of the similar P2-type material, in which iron replaces aluminum.[20] Furthermore, the refined occupancy values for the two Na sites as well as Mn, Ni, Al occupancies are in good agreement with the $Na_{0.6}Ni_{0.22}Al_{0.11}Mn_{0.66}O_2$ composition determined by ICP-OES. It is noteworthy that the large B_{iso} values for sodium sites determined by the refinement indicate vacant sodium prismatic sites, thus suggesting a fast sodium-ion diffusion in the host structure.[34]

Figure 1

Table 1

The morphological properties of the material, as pristine powder and composite electrode mixture, have been investigated by scanning electron microscopy (Fig. 2). The micrograph of the pristine powder (Fig. 2a) shows a flake-like morphology with a primary particle size ranging from 3 to 5 µm (see Fig. 2a). At higher magnification (Fig. 2b) the material reveals adherent planes well reflecting the defined layered structure. The SEM analysis has been extended to the dried composite electrode slurry composed of the active material ($Na_{0.6}Ni_{0.22}Al_{0.11}Mn_{0.66}O_2$), carbon black conductive agent and binder (Fig. 2 c and d). The enhanced electronic conductivity of the composite, promoted by the carbon conductor, i.e., the black round-shaped particles clearly surrounding the active material in the SEM image, enables the

identification of the hexagonal symmetry and the observation of the plate-like sub-micrometric primary particles.

Figure 2

The elemental mapping by energy dispersive X-ray spectroscopy of Na, Mn, Ni, Al and O, reported in the Supplementary Information (SI) section (Fig. S1) reveals the metal distribution in the $Na_{0.6}Ni_{0.22}Al_{0.11}Mn_{0.66}O_2$. The analysis reveals the homogeneous distribution of the metals with the exception of aluminum showing a spot-like agglomeration. In order to clarify this anomaly, the EDX analysis was performed on a pre-annealed precursor of the material composed by a mixture of $Ni_{0.22}Al_{0.11}Mn_{0.66}(OH)_2$ and NaOH. The results, reported in Fig. S2 in the SI section, clearly shows homogeneous distribution of the metals, including Al. Hence, we may propose that aluminum agglomeration is mainly driven by the final annealing step of the synthesis conducted at 1000 °C under air atmosphere, possibly leading to the formation of Al_2O_3 based compounds. Despite these results may in principle suggest a phase separation into an aluminum-rich compound, the XRD characterization reported in Figure 1 and the related phase quantification reveal absence of side products, but only the formation of the pure P2-type $Na_{0.6}Ni_{0.22}Al_{0.11}Mn_{0.66}O_2$ compound. Indeed, the formation of an aluminum oxide impurity, i.e., below the XRD detection limit, cannot be excluded. The inhomogeneous distribution of aluminum in layered compounds may not be excluded, as suggested in literature by asymmetric 101 peak in the diffraction pattern of $LiNi_{0.7}Co_{0.1}Al_{0.2}O_2$ doped compound.[35] However, a more specific study is certainly required to fully clarify this aspect.

The evaluation of the $Na_{0.6}Ni_{0.22}Al_{0.11}Mn_{0.66}O_2$ electrochemical behavior has been performed by cyclic voltammetry (Fig. 3). The voltammogram shows three main redox processes associated to the sodium intercalation within the host structure, occurring in the 1.5-4.6 V potential range. The Mn^{3+}/Mn^{4+} redox process evolves at about 2.0 V (green circle), corresponding to high sodium content within the layered structure. The redox activity of Mn^{3+}/Mn^{4+} may be also accompanied by a phase transition driven by a

Jahn-Teller cooperative effect from a P2 to a P'2 (i.e., from hexagonal to orthorhombic phase).[21] At higher potential values, i.e., from 3.1 V to 3.7 V, the Ni^{2+}/Ni^{4+} two-electrons redox reaction occurs (blue circle).[20,23,36] A further decrease of the sodium content in the layered structure, occurring at potentials higher than 4.0 V, leads to the phase transition from a P to an O stacking (red circle), corresponding to the energetically favored misalignment along the c-axis of oxygen atoms belonging to adjacent transition metal layers.[17,21,23,29]

The voltammograms in Fig. 3 reveal the excellent reversibility and profile retention of the sodium intercalation process ascribed to the nickel redox reaction at intermediate potentials (3.1 V to 3.7 V), as well as the shape modification and decreasing magnitude of the peaks associated to the redox processes at low (2.0 V) and high (4.2 V) potential values, involving structural modification and phase transition, respectively. However, the positive effects of aluminum inclusion into the layered structure are demonstrated by Fig. S3 in SI section, which compares the voltammetry profiles of $Na_{0.6}Ni_{0.22}Al_{0.11}Mn_{0.66}O_2$ and $Na_{0.6}Ni_{0.22}Fe_{0.11}Mn_{0.66}O_2$ materials.[20,36] The figure reveals higher peak resolution, lower polarization and enhanced stability, thus suggesting faster kinetics and improved reversibility of the sodium intercalation electrochemical processes, as well as an enhanced structural stability of the aluminum-doped compound. The most relevant difference may be observed within the high potential region corresponding to the P2-O2 phase transition. Indeed, $Na_{0.6}Ni_{0.22}Fe_{0.11}Mn_{0.66}O_2$ shows an irreversible process at 4.2 V, while $Na_{0.6}Ni_{0.22}Al_{0.11}Mn_{0.66}O_2$ evidences at the same potential a reversible trend, with an oxidation peak centered at 4.26 V and a reverse reduction peak at 4.1 V, thus suggesting a key role of aluminum in stabilizing the layered structure and enhancing its electrochemical process in sodium cell. The differences observed in the cyclic voltammetry of $Na_{0.6}Ni_{0.22}Fe_{0.11}Mn_{0.66}O_2$ [20] and the $Na_{0.6}Ni_{0.22}Al_{0.11}Mn_{0.66}O_2$ at voltages higher than 4.0V indicate that the aluminum inclusion affects the de-sodiation ability, in particular during the first cycle. Indeed, $Na_{0.6}Ni_{0.22}Fe_{0.11}Mn_{0.66}O_2$ shows a first charge capacity of about 120 mAh g^{-1} [20], while $Na_{0.6}Ni_{0.22}Al_{0.11}Mn_{0.66}O_2$ approaches 160

mAh g^{-1} (see following paragraph). The improved sodium exchange ability by aluminum doping is expected to enhance the overall electrochemical behavior, both in terms of delivered capacity and reversibility as indeed demonstrated by the tests in sodium cell.

Figure 3

The electrochemical behavior of the $Na_{0.6}Ni_{0.22}Al_{0.11}Mn_{0.66}O_2$ material in sodium cell is investigated by galvanostatic cycling within the 1.5-4.6 V. Fig. 4 shows the cycling behavior (a) and the voltage profile (b) of the cell obtained at a constant current value of 20 mA g^{-1}. The first charge process (Fig. 4a) leads to a capacity of about 160 mAh g^{-1} which indicates the complete removal of 0.6 equivalent of sodium from the layered structure. During the first discharge process, the capacity rises to 252 mAh g^{-1}, and the amount of sodium intercalated in the structure increases to 0.9 equivalent, reflecting the behavior of the sodium deficient but thermodynamically stable P2-type phase. The following cycles (Fig. 4b) evidence the remarkable reversible capacity of about 250 mAh g^{-1}, to the best of our knowledge never reported before, making this material suitable for high energy SIBs. Although the cycling test shows a progressive decay, ascribed to the phase changes and structural reorganization earlier discussed, a still high value of about 200 mAh g^{-1} (80% of the initial value) is maintained upon the 50 cycles considered in the test. The rate performance test of $Na_{0.6}Ni_{0.22}Al_{0.11}Mn_{0.66}O_2$ was performed by galvanostatic cycling with currents increasing from 1C to 5C. The voltage profiles of Fig. 4c reveal the expected signature of the layered material with modest increase of the polarization until 2C, while the cycling trend of Fig. 4d evidences reversible capacities of about 220 mAh g^{-1} at 0.1 C (10^{th} cycle), 207 mAh g^{-1} at 0.2 C (15^{th} cycle), 190 mAh g^{-1} at 0.5C (20^{th} cycle), 178 mAh g^{-1} at 1C (25^{th} cycle), 163 mAh g^{-1} 2C (30^{th} cycle) and 140 mAh g^{-1} at 5C (35^{th} cycle). Moreover, the cell can recover about 91% of the initial capacity by decreasing the current from 5C back to 0.1C. These characteristics, in particular the remarkably high delivered capacity, are very promising for the application of the material as cathode in sodium ion batteries.

Figure 4

The structural and morphological evolution upon cycling of the $Na_{0.6}Ni_{0.22}Al_{0.11}Mn_{0.66}O_2$ electrode within the 1.5-4.6 V range has been evaluated by ex-situ SEM and XRD. Fig. 5 shows the galvanostatic voltage profile of the Na/ PC, 1M $NaPF_6$ / $Na_{0.6}Ni_{0.22}Al_{0.11}Mn_{0.66}O_2$ cell. The circles indicate the various states of charge at which SEM (Fig. 5 panels *a-d*) and XRD (Fig. 5 panels *a'-d'*) analyses were performed. The SEM images of the electrode at the open circuit voltage (Fig. 5, panel *a*) shows the expected morphology characterized by adherent planes composed by flake-like particles, while the corresponding XRD pattern (Fig. 5, panel *a'*) can be indexed as the P2-type structure belonging to the hexagonal $P6_3/mmc$ space group. The SEM image of the electrode fully charged up to 4.6V (Fig. 5, panel *a*) evidences the remarkable increase of the interlayer space within the material flakes due to sodium removal, and consequent increased repulsion between the adjacent oxygen atoms, as well as to water uptake during the analysis of the sensitive de-sodiated layered oxide.[30,37]. Accordingly, the XRD pattern of the fully charged electrode (Fig. 5, panel *b'*) shows a new broad peak at about 18.7 degree of 2θ due to the gliding of MO_2 layers which imposes an octahedral environment to sodium ions. Isostructural P2-$Na_xNi_{1/3}Mn_{2/3}O_2$ material may undergo transformation into O2-type structure upon sodium removal ($x < 1/3$).[29] Theoretical calculations suggest the largest difference of formation energy between P2 structure and O2 structures to occur in correspondence to $x = 0$, since the *c* axis significantly decreases in the fully de-sodiated O2-$Ni_{1/3}Mn_{2/3}O_2$ phase.[28] Literature work on de-sodiated P2-$Na_xFe_{0.5}Mn_{0.5}O_2$ evidenced the shift of the 002 reflection from about 15 to 17 degree of 2θ, suggesting the formation of O/P stacking mixture indexed with an OP4 structure.[17] Further studies on nickel-substituted P2-$Na_xFe_{0.5}Mn_{0.5}O_2$ proposed a "Z" phase [21] with relevant structural reorganization during de-sodiation, most likely related to the displacement of the transition metal atoms perpendicularly to the hexagonal lattice.[23] However, the poor crystallinity of the de-sodiated phase so far hindered proper XRD characterization. The disappearance of the 00l reflections and the appearance of the new peak at higher angles upon full de-sodiation observed in our study indicate a shrinkage of the *c* lattice parameter and a complete transition

from a P to an O stacking type arrangement. The phase transformation occurs with a gliding of layers by following two possible directions, *i.e.*, regular gliding from AB BA AB BA oxygen stacking to AB CB AB CB or AB AC AB AC stacking to form the O2 structure, and irregular gliding leading to the O4 structure.[29] However, stacking faults, suggested by peaks broadening, hinder the indexing to the O2 or O4 structure. Our XRD analysis indicates the formation of a close packed configuration with octahedral vacancies. The XRD pattern of the fully charged electrode (Fig. 5, panel *b'*) exhibits two additional peaks at about 12.5° and 25° of 2θ. The peaks may be attributed to the appearance of a hydrated phase, and could be indexed as 002' and 004' deriving from the shift of the 002 and 004 peaks of the P2-phase upon water intercalation.[37] The high water sensitivity of sodium-based transition metal layered oxides with general formula Na_xMO_2, facilitated when $x < 0.34$, may reasonably explain the appearance of hydrated phase, in which water molecules may partially replace sodium vacancies in the fully de-sodiated state even under controlled atmosphere (i.e., glove box containing only traces of H_2O).[38] Furthermore, the hydrated phase formed by contamination of the material during the ex-situ measurements shows reversible water up-take upon electrode heating as shown in Fig. S4 (Supplementary Information).

The phase change occurring upon first charge appears fully reversible upon discharge, as clearly demonstrated by the micrograph of the electrode discharged down to 2.0 V (Fig. 5 panel *c* shows) and corresponding XRD pattern (Fig. 5, panel *c'*). Further discharge down to 1.5V, corresponding to sodium contents greater than 0.8 eq of Na per formula unit, leads to the phase transition from the hexagonal P2 (*$P6_3/mmc$* space group) to the orthorhombic P'2 (*Cmcm* space group) promoted by the Jahn-Teller effect of the active Mn^{3+} ions. In fact, Fig. 5 (panel *d'*) reveals that the (002) peak shifts to a lower angle due to increased *c* lattice parameter.[21] Further details are revealed by the magnification of the XRD patterns at various state of charge section in Fig. S4 (Supplementary Information). The corresponding SEM image (Fig. 5, panel *d*) shows the appearance of a thin layer covering the electrode surface, mostly due to electrolyte decomposition occurring upon discharge at lower voltages (i.e., 1.5 V). In summary, the

structural and morphological changes observed (Fig. 5) match with the electrochemical behavior of the material upon the cycling tests reported in Figs. 3 and 4.

Figure 5

An attempt to improve the electrode stability consists in limiting the electrode voltage excursion in order to control the occurrence of phase changes and associated structural modifications. The 2^{nd} and 50^{th} cycles recorded from several cells galvanostatically (20 mA g^{-1}) cycled within the various cut off voltages are reported in Fig. 6. In Table 2 are summarized the delivered capacity, cycling stability, coulombic and voltage efficiency obtained. The average working voltages reported in Table 2 have been calculated by dividing the total energy density of the cell (integral of the voltage *vs.* specific capacity curve) by the specific capacity measured at the end of charge and discharge at different voltage values.

Figure 6 (a and c) reports the cell response in terms of voltage profile and cycling behavior with the lower cut off voltage fixed at 1.5 V. Three different upper cut off voltages were investigated in order to analyze the influence of electrolyte decomposition (1.5-4.6 V, see panel I Fig.6 a), the effect of the P-O phase transition without the influence of electrolyte decomposition (1.5-4.3 V see panel II Fig.6 a) and finally the influence of the low voltage structural rearrangement likely due to Mn dissolution, avoiding both the P-O phase transition and the electrolyte decomposition (1.5-4.0 V, see panel III Fig.6 a).

The same measurements, Fig. 6 (b and d), were conducted cutting out the Mn^{4+}/Mn^{3+} redox process, i.e., fixing the lower cut off voltage of 2.0 V. Indeed, avoiding the Mn redox process allows for a deeper analysis on the high voltage cut off because it avoids the low voltage material's degradation.

Panels (I) and (II) in Figure 6a show that the effect of electrolyte decomposition on the capacity retention is not substantial. In fact, the capacity retention after 50 cycles (see Figure 6c green and red dots curves) is rather similar, i.e., 79.46% and 81.30% with upper cut off voltage of 4.6 and 4.3 V, respectively (see Table 2). However, the coulombic efficiency of the process is improved, since irreversible oxidative decomposition processes borne by the electrolyte are avoided. As shown in Fig. 6b the same results are

obtained when increasing the low voltage cut off at 2.0 V (compare the cycling performance in the 2.0-4.6 V and 2.0-4.3 V voltage ranges in Table 2). The major difference observed refers to the average working voltage and voltage efficiency upon cycling. The cell cycled up to 4.6 V shows an initially higher average voltage value, however, it is also affected by a stronger voltage decay.

Panels (III) of Fig. 6 show, respectively, the voltage profiles of the cells cycled within 1.5-4.0 V and 2.0-4.0 V voltage ranges, i.e., avoiding the P-O phase transition. Here, two main differences are observed. In the first case, the average working voltage is about 2.5 V while the 1st discharge capacity is 183 mAh g^{-1}. In the second case, the values are, respectively, 2.9 V and 77 mAh g^{-1}. However, the cells showed rather different capacity retention after 50 cycles (about 93% and 100%, respectively), pointing out the key role of manganese redox reaction in the material's cycling behavior. Indeed, as previously discussed (Fig. 5 and related text), the increased concentration of Jahn-Teller active Mn^{3+} leads to a distortion of the host structure responsible of the capacity decay upon cycling, also involving manganese dissolution. With respect to voltage efficiency, however, the best performance in terms of voltage efficiency are offered by the cells cycled in the 1.5-4.0 V and 2.0-4.0 V ranges, thus indicating that the high voltage process influences the voltage fade more than the manganese redox process.

Summarizing, me may assume that the high voltage phase transition is deleterious in terms of voltage decay upon cycling while manganese redox activity plays a fundamental role in the long-term cycling stability of layered oxides (see Fig. S5). Previous studies underlined the importance of a proper voltage window for the improvement of the cycling behavior. It has been suggested that the cycling performance of $Na_{2/3}Fe_{1/2}Mn_{1/2}O_2$ can be enhanced by controlling the phase evolution. Limiting the voltage window to 2.0-4.0 V may lead to satisfactory retention, however, to modest delivered capacity. [39] Further studies suggested 4.0-2.1 V as suitable voltage range for $Na_x[Mn_{0.5}Fe_{0.5}]O_2$, while the beneficial effect of nickel substitution led to a wider stability window (i.e., 4.1-2.0 V) for the $Na_x[Mn_{0.65}Ni_{0.15}Fe_{0.2}]O_2$ compound.[23] In this study, the higher amount of nickel within the layered structure and the well-balanced metal

intermixing have raised up to 2.0-4.3 V the optimal operating voltage window, which represents a compromise between cycling stability and delivered capacity (see Fig. S5). Furthermore, cycling within 2.0V and 4.0V led to excellent cycling performance, extended over 200 cycles, although with lower capacity.

Figure 6

Table 2

In order to further analyze processes affecting the electrochemical performance, the increase of the cell resistance, attributed to electrolyte's degradation, and structural changes, leading to loss of hosting sites for sodium, have been investigated by means of electrochemical impedance analysis.

Fig. 7a displays the voltage profile of the Na/PC, 1M $NaPF_6$/NAM cell cycled at 20 mA g^{-1} within the 4.6-1.5 V potential range, with circles indicating the EIS measurements used to monitor the electrode impedance change by varying its state of charge. The corresponding Nyquist plots reported in Fig. 7b and c display the electrolyte resistance intercept at the highest frequencies (see insets), a first small semicircle at high frequency due to solid electrolyte interface (SEI) layer film formation and electrodes passivation, followed by a second medium frequency semicircle attributed to the sodium charge transfer process.[40–43] At very low frequency, a final semi-infinite line due to sodium ions solid-state diffusion is displayed for the pristine electrode (OCV) and for electrodes charged at 3.7 V and 4.2 V.[41] The charge transfer semicircle increases and the final line sags by charging the cell up to 4.6V (Fig. 7a). This may be ascribed to the remarkable decrease of the electronic conductivity of the electrode at very low sodium content, as indeed confirmed by the ohmic drop from 4.6 V at the end of the charge to about 4.1 V at the beginning of the discharge (Fig. 7a), suggesting an insulating character of the de-sodiated phase.[44,45] Further discharge to 3.7 V leads to a decrease of the cell resistance with impedance spectra well comparing the one obtained by charging the cell at the same voltage value (compare figs. 7c and 7b). The discharge process down to 2.0 V results in an increase of the resistance due to electrolyte reductive

decomposition and partial SEI film formation (see corresponding SEM image in panel III of Fig. 5). Full discharge down to 1.5 V (Fig. 7c) reveals an impedance spectra characterized by a small semicircle at the high frequency region due to a compact SEI film formation (see corresponding SEM image in panel IV of Fig. 5), and to a tilted line bending to high values of resistance by decreasing the frequency, due to possible blocking character of the electrode or to partially insulating nature of the SEI film.[46]

Figure 7

4. Conclusions

We have synthesized a P2-type $Na_{0.6}Ni_{0.22}Al_{0.11}Mn_{0.66}O_2$ electrode characterized by a remarkably high capacity by incorporating low atomic mass aluminum into the layered structure of the nickel-manganese based oxide. The results herein reported suggest that aluminum plays a key role in determining the electrochemical performances, and point out the role of the transition metal involved in the host structure. The amount of sodium being (de-)intercalated (i.e., about 0.9 equivalent) corresponds to a capacity value as high as 252 mAh g^{-1}, and represents a very promising property for application of the cathode in high performance SIBs. In operando SEM, XRD and EIS data suggest that both electrolyte decomposition and phase transitions play important role in determining the electrode activity at very low and high sodium intercalation degree. Indeed, the increase of the overall cell resistance in the fully charge and discharge state may be attributed to the morphological and structural properties of the material. The low conductivity of the high voltage phase may be related to the appearance of O-stacking within the P-type structure, as pointed out by ex-situ XRD analysis. Despite additional specific studies focused on the solid/electrolyte interphase properties and the characteristics of the phase transitions are required to fully understand and optimize the electrode behavior, the material here reported may be considered a very promising candidate for application as high capacity cathode in sodium-ion batteries.

Acknowledgments

IH and SP thank the financial support of the European Commission within the FP7- ENERGY-2013-1 Project INFLUENCE (Grant number: 608621). IMERYS and ARKEMA are acknowledged for kindly providing Super C and PVdF, respectively. J.H. thanks the collaboration project "Accordo di Collaborazione Quadro 2015" between the University of Ferrara (Department of Chemical and Pharmaceutical Sciences) and Sapienza University of Rome (Chemistry Department).

References

1 V. Palomares, P. Serras, I. Villaluenga, K. B. Hueso, J. Carretero-González and T. Rojo, *Energy Environ. Sci.*, 2012, **5**, 5884–5901.

2 M. Sawicki and L. L. Shaw, *RSC Adv.*, 2015, **5**, 53129–53154.

3 D. Kundu, E. Talaie, V. Duffort and L. F. Nazar, *Angew. Chemie Int. Ed.*, 2015, **54**, 3431–3448.

4 N. Yabuuchi, K. Kubota, M. Dahbi and S. Komaba, *Chem. Rev.*, 2014, **114**, 11636–11682.

5 H. Pan, Y.-S. Hu and L. Chen, *Energy Environ. Sci.*, 2013, **6**, 2338–2360.

6 K. Kubota, N. Yabuuchi, H. Yoshida, M. Dahbi and S. Komaba, *MRS Bull.*, 2014, **39**, 416–422.

7 F. Sanz, C. Parada, J. M. Rojo and C. Ruíz-Valero, *Chem. Mater.*, 2001, **13**, 1334–1340.

8 I. Hasa, J. Hassoun, Y. K. Sun and B. Scrosati, *ChemPhysChem*, 2014, **15**, 2152–2155.

9 Y. Lu, L. Wang, J. Cheng and J. B. Goodenough, *Chem. Commun.*, 2012, **48**, 6544–6546.

10 L. Wang, Y. Lu, J. Liu, M. Xu, J. Cheng, D. Zhang and J. B. Goodenough, *Angew. Chemie Int. Ed.*, 2013, **52**, 1964–1967.

11 J. Song, L. Wang, Y. Lu, J. Liu, B. Guo, P. Xiao, J.-J. Lee, X.-Q. Yang, G. Henkelman and J. B. Goodenough, *J. Am. Chem. Soc.*, 2015, **137**, 2658–2664.

12 P. Xiao, J. Song, L. Wang, J. B. Goodenough and G. Henkelman, *Chem. Mater.*, 2015, **27**,

3763–3768.

13 C. Masquelier and L. Croguennec, *Chem. Rev.*, 2013, **113**, 6552–6591.

14 Y. H. Jung, C. H. Lim and D. K. Kim, *J. Mater. Chem. A*, 2013, **1**, 11350–11354.

15 C. Delmas, C. Fouassier and P. Hagenmuller, *Phys. B+C*, 1980, **99**, 81–85.

16 M. H. Han, E. Gonzalo, G. Singh and T. Rojo, *Energy Environ. Sci.*, 2015, **8**, 81–102.

17 N. Yabuuchi, M. Kajiyama, J. Iwatate, H. Nishikawa, S. Hitomi, R. Okuyama, R. Usui, Y. Yamada and S. Komaba, *Nat. Mater.*, 2012, **11**, 512–517.

18 D. Kim, E. Lee, M. Slater, W. Lu, S. Rood and C. S. Johnson, *Electrochem. commun.*, 2012, **18**, 66–69.

19 I. Hasa, D. Buchholz, S. Passerini, B. Scrosati and J. Hassoun, *Adv. Energy Mater.*, 2014, **4**, 10.1002/aenm.201400083.

20 I. Hasa, D. Buchholz, S. Passerini and J. Hassoun, *ACS Appl. Mater. Interfaces*, 2015, **7**, 5206–5212.

21 B. Mortemard de Boisse, D. Carlier, M. Guignard, L. Bourgeois and C. Delmas, *Inorg. Chem.*, 2014, **53**, 11197–205.

22 J. Billaud, G. Singh, a R. Armstrong, E. Gonzalo, V. Roddatis, M. Armand, T. Rojo and P. G. Bruce, *Energy Environ. Sci.*, 2014, **7**, 1387–1391.

23 E. Talaie, V. Duffort, H. Smith, B. Fultz and L. Nazar, *Energy Environ. Sci.*, 2015, **8**, 2512–2523.

24 R. Berthelot, D. Carlier and C. Delmas, *Nat. Mater.*, 2011, **10**, 74–80.

25 Y. Wang, R. Xiao, Y.-S. Hu, M. Avdeev and L. Chen, *Nat. Commun.*, 2015, **6**, 6954.

26 R. J. Clément, P. G. Bruce and C. P. Grey, *J. Electrochem. Soc.*, 2015, **162**, A2589–A2604.

27 J. A. Saint, M. M. Doeff and J. Wilcox, *Chem. Mater.*, 2008, **20**, 3404–3411.

28 D. H. Lee, J. Xu and Y. S. Meng, *Phys. Chem. Chem. Phys.*, 2013, **15**, 3304–12.

29 Zhonghua Lu and J. R. Dahn, *J. Electrochem. Soc.*, 2001, **148**, A1225–A1229.

30 V. Duffort, E. Talaie, R. Black and L. F. Nazar, *Chem. Mater.*, 2015, **27**, 2515–2524.

31 Y. Li, Z. Yang, S. Xu, L. Mu, L. Gu, Y.-S. Hu, H. Li and L. Chen, *Adv. Sci.*, 2015, **2**, 10.1002/advs.201500031.

32 G. Singh, N. Tapia-Ruiz, J. M. Lopez del Amo, U. Maitra, J. W. Somerville, A. R. Armstrong, J. Martinez de Ilarduya, T. Rojo and P. G. Bruce, *Chem. Mater.*, 2016, **28**, 5087–5094.

33 H. Yoshida, N. Yabuuchi, K. Kubota, I. Ikeuchi, A. Garsuch, M. Schulz-Dobrick and S. Komaba, *Chem. Commun.*, 2014, **50**, 3677–3680.

34 N. Yabuuchi, R. Hara, K. Kubota, J. Paulsen, S. Kumakura and S. Komaba, *J. Mater. Chem. A*, 2014, **2**, 16851–16855.

35 S. Madhavi, G. V Subba Rao, B. V. R. Chowdari and S. F. Y. Li, *J. Power Sources*, 2001, **93**, 156–162.

36 D. Yuan, X. Hu, J. Qian, F. Pei, F. Wu, R. Mao, X. Ai, H. Yang and Y. Cao, *Electrochim. Acta*, 2014, **116**, 300–305.

37 Z. Lu and J. R. Dahn, *Chem. Mater.*, 2001, **13**, 1252–1257.

38 D. Buchholz, L. G. Chagas, C. Vaalma, L. Wu and S. Passerini, *J. Mater. Chem. A*, 2014, **2**, 13415–13421.

39 W. K. Pang, S. Kalluri, V. K. Peterson, N. Sharma, J. Kimpton, B. Johannessen, H. K. Liu, S. X. Dou and Z. Guo, *Chem. Mater.*, 2015, **27**, 3150–3158.

40 M. D. Levi, G. Salitra, B. H. Markovsky Teller, D. Aurbach, U. Heider and L. Heider, *J. Electrochem. Soc.*, 1999, **146**, 1279–1289.

41 M. D. Levi, K. Gamolsky, D. Aurbach, U. Heider and R. Oesten, *Electrochim. Acta*, 2000, **45**, 1781–1789.

42 F. Orsini, M. Dolle and J. M. Tarascon, *Solid State Ionics*, 2000, **135**, 213–221.

43 R. Ruffo, R. Fathi, D. J. Kim, Y. H. Jung, C. M. Mari and D. K. Kim, *Electrochim. Acta*, 2013, **108**, 575–582.

44 F. Nobili, S. Dsoke, F. Croce and R. Marassi, *Electrochim. Acta*, 2005, **50**, 2307–2313.

45 F. Nobili, S. Dsoke, M. Minicucci, F. Croce and R. Marassi, *J. Phys. Chem. B*, 2006, **110**, 11310–11313.

46 J.-B. Jorcin, M. E. Orazem, N. Pébère and B. Tribollet, *Electrochim. Acta*, 2006, **51**, 1473–1479.

Table Captions

Table 1. Structural parameters and summary of the refined parameters of the $Na_{0.6}Ni_{0.22}Al_{0.11}Mn_{0.66}O_2$ P2-type phase.

Table 2. Summary of key parameters investigated during the cycling tests reported in Figure 6. The significant values in terms of specific discharge capacity, capacity retention, coulombic efficiency, average discharge/charge potential and voltage efficiency have been extracted and calculated for the six potential ranges investigated.

Figure Captions

Figure 1. Experimental (black line) and calculated (red line) X-ray diffraction patterns of the $Na_{0.6}Ni_{0.22}Al_{0.11}Mn_{0.66}O_2$ cathode material. The inset reports a schematic illustration of the P2-type structure as obtained by the refined cell parameters.

Figure 2. SEM micrographs at various magnifications of the P2-$Na_{0.6}Ni_{0.22}Al_{0.11}Mn_{0.66}O_2$ material in the pristine powder state (a,b) and upon mixing with carbon black conductive agent and binder (c,d).

Figure 3. Cyclic voltammetry profiles of $Na_{0.6}Ni_{0.22}Al_{0.11}Mn_{0.66}O_2$ electrode in a three-electrode sodium cell using 1M $NaPF_6$-PC electrolyte. Measurement performed at 0.1mV sec^{-1} scan rate within the 4.6-1.5

V vs Na/Na^+ potential range. Circles indicate the peaks ascribed to main redox processes occurring during the voltammetry test. Temperature: 20 ± 2 °C.

Figure 4. Cycling trend (a) and voltage profile (b) of a Na/PC, 1M $NaPF_6$/P2-$Na_{0.6}Ni_{0.22}Al_{0.11}Mn_{0.66}O_2$ cell galvanostatically characterized at a current value of 20 mA g^{-1} within the 4.6-1.5 V vs Na/Na^+ potential range. Rate capability cycling behavior (c) and selected voltage profiles (d) of the sodium cell studied at various current rates. Temperature: 20 ± 2 °C.

Figure 5. Voltage profile of the Na/P2-$Na_{0.6}Ni_{0.22}Al_{0.11}Mn_{0.66}O_2$ cell galvanostatically cycled at 20 mA g^{-1} in 1 M $NaPF_6$-PC electrolyte. Circles indicate the state of charge of the cell corresponding to the ex situ SEM and XRD analyses of the electrode performed upon cycling. SEM micrographs (panels *a-d* and XRD patterns (panels *a'-d'*) of the pristine electrode (orange circle, panel *a* and *a'*), fully-charged electrode (blue circle, de-sodiated at 4.6 V, panels *b* and *b'*), partially discharged (green circle, sodiated down to 2.0 V, panels *c* and *c'*) and fully discharged electrode (red circle, sodiated down to 1.5 V, panels *d* and *d'*).

Figure 6. Galvanostatic charge/discharge profiles of selected cycles of Na/P2-$Na_{0.6}Ni_{0.22}Al_{0.11}Mn_{0.66}O_2$ cells performed at 20 mA g^{-1} within various voltage ranges, changing the upper voltage cut off and fixing the lower one at 1.5 V vs Na/Na^+ (a) and at 2.0 V vs Na/Na^+ (b). The corresponding cycling behavior is displayed in panels (c) and (d).

Figure 7. (a) Voltage profile of the first galvanostatic (de-)sodiation process of the $Na_{0.6}Ni_{0.22}Al_{0.11}Mn_{0.66}O_2$ electrode in sodium cell performed within the 4.6-1.5 V range at a current of 20 mA g^{-1}. Circles indicate the state of charge corresponding to impedance measurement. (b) Nyquist plots during first charge and (c) during first discharge of the $Na_{0.6}Ni_{0.22}Al_{0.11}Mn_{0.66}O_2$ electrode in sodium half-cell. Magnifications at the high frequency region are reported as insets. Temperature: 20 ± 2 °C.

Lattice		Space group	a [Å]	c [Å]	V [Å^3]	R_{wp} / GOF
Hexagonal		$P6_3/mmc$	2.8737(1)	11.203(6)	80.121(4)	11.28 / 1.22
Atom	**Wyckoff**	**x**	**y**	**z**	**Occupancy**	**B_{iso} [Å^2]**
Mn	2*a*	0	0	0	Mn^{4+} 0.672(9)	0.67(1)
Ni	2*a*	0	0	0	Ni^{2+} 0.249(8)	0.67(1)
Al	2*a*	0	0	0	Al^{3+} 0.109(2)	0.67(1)
Na(1)=Na_f	2*b*	0	0	0.25	Na^+ 0.238(1)	4.03(6)
Na(2)=Na_e	2*d*	0.3333	0.6667	0.75	Na^+ 0.330(1)	3.95(4)
O	4*f*	0.3333	0.6667	0.0829(6)	O^{2-} 1	0.87(5)

Table 1

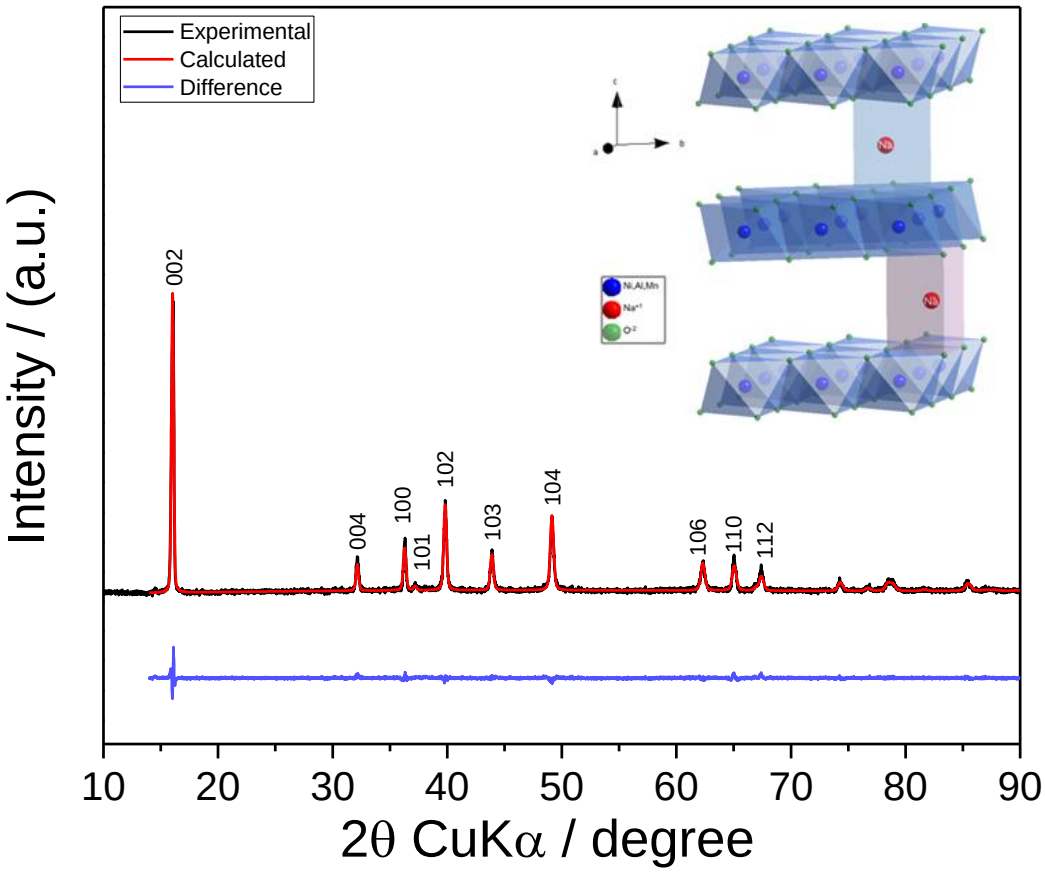
Experimental
Calculated
Difference
002
004
100
101
102
103
104
106
110
112
Intensity / (a.u.)
10
20
30
40
50
60
70
80
90
2θ CuKα / degree

Figure 1

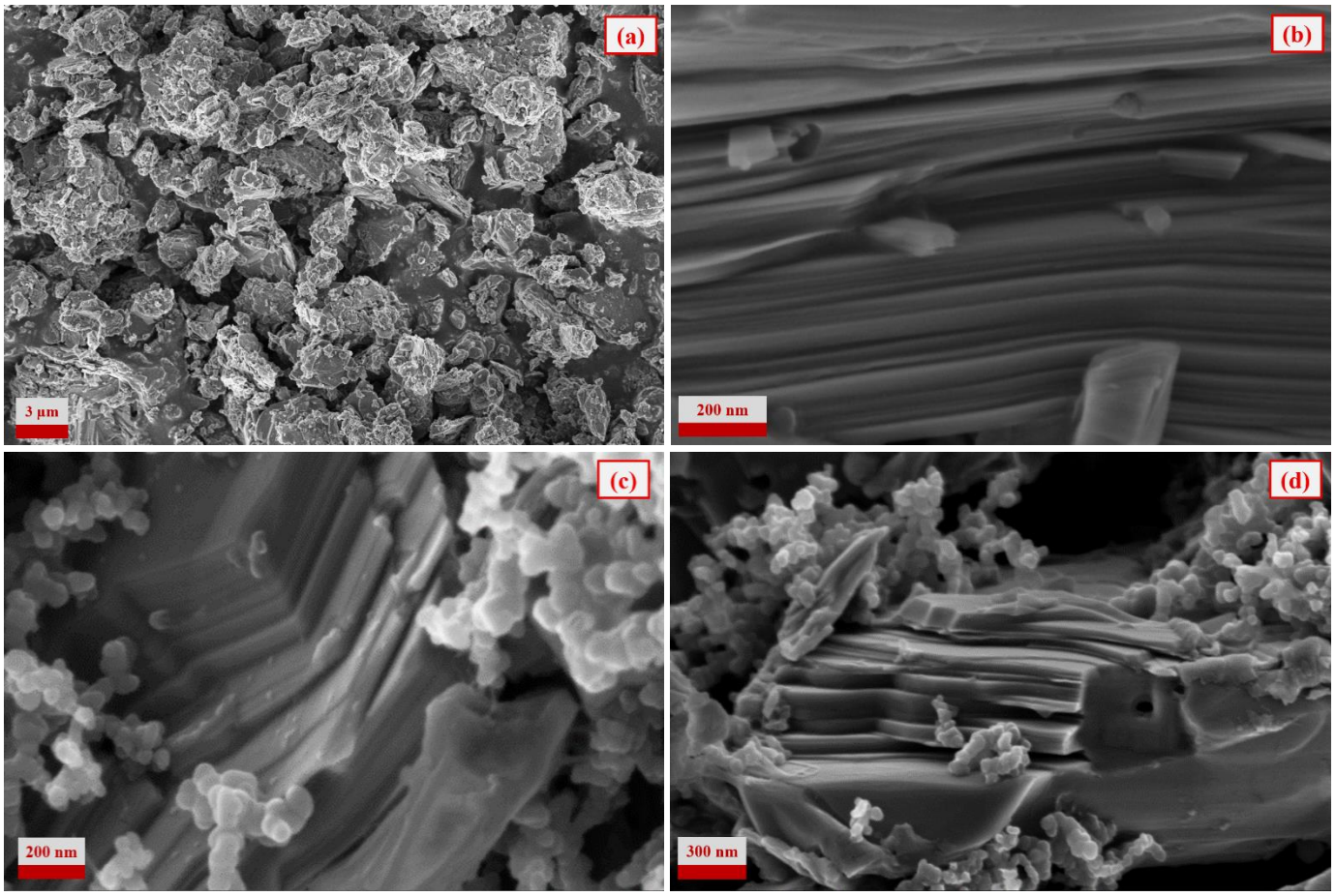

Figure 2

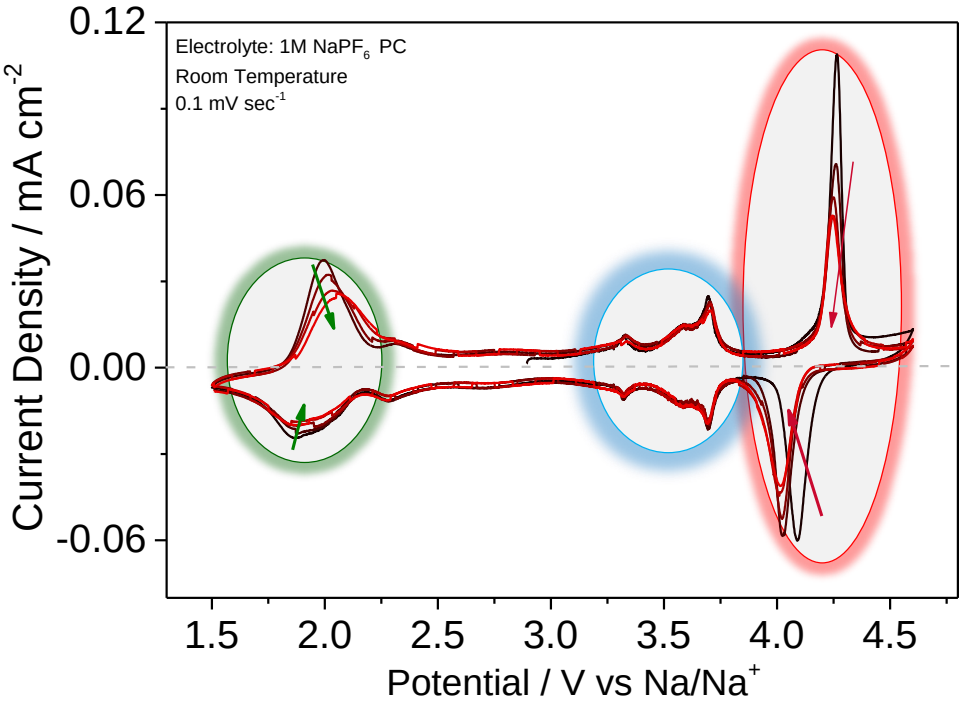
Electrolyte: 1M NaPF6 PC
Room Temperature
0.1 mV sec-1
Current Density / mA cm-2
0.12
0.06
0.00
-0.06
1.5
2.0
2.5
3.0
3.5
4.0
4.5
Potential / V vs Na/Na+

Figure 3

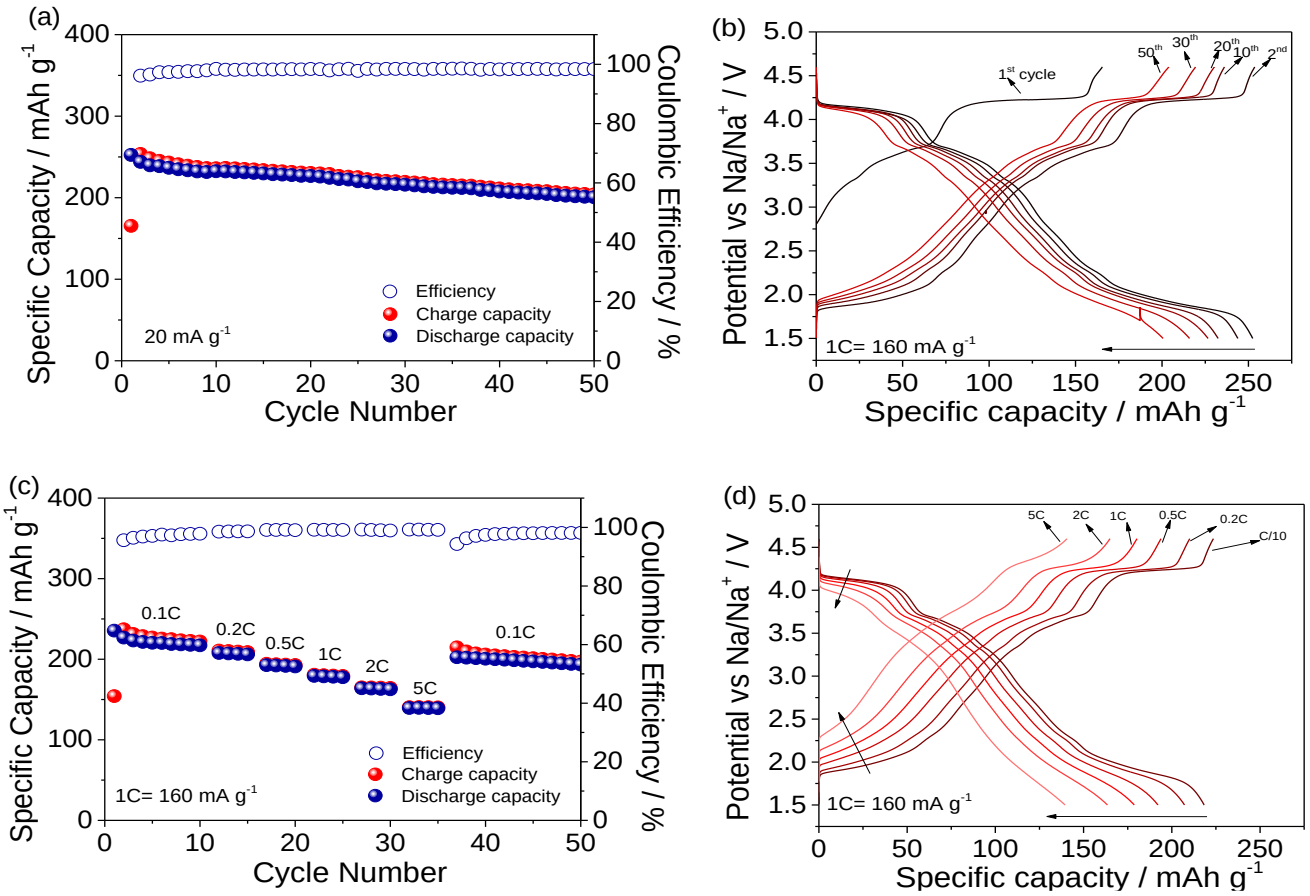
(a)
Specific Capacity / mAh g-1
Coulombic Efficiency / %
Cycle Number
20 mA g-1
Efficiency
Charge capacity
Discharge capacity
(b)
Potential vs Na/Na+ / V
Specific capacity / mAh g-1
1st cycle
50th
30th
20th
10th
2nd
1C= 160 mA g-1
(c)
Specific Capacity / mAh g-1
Coulombic Efficiency / %
Cycle Number
0.1C
0.2C
0.5C
1C
2C
5C
0.1C
1C= 160 mA g-1
Efficiency
Charge capacity
Discharge capacity
(d)
Potential vs Na/Na+ / V
Specific capacity / mAh g-1
5C
2C
1C
0.5C
0.2C
C/10
1C= 160 mA g-1

Figure 4

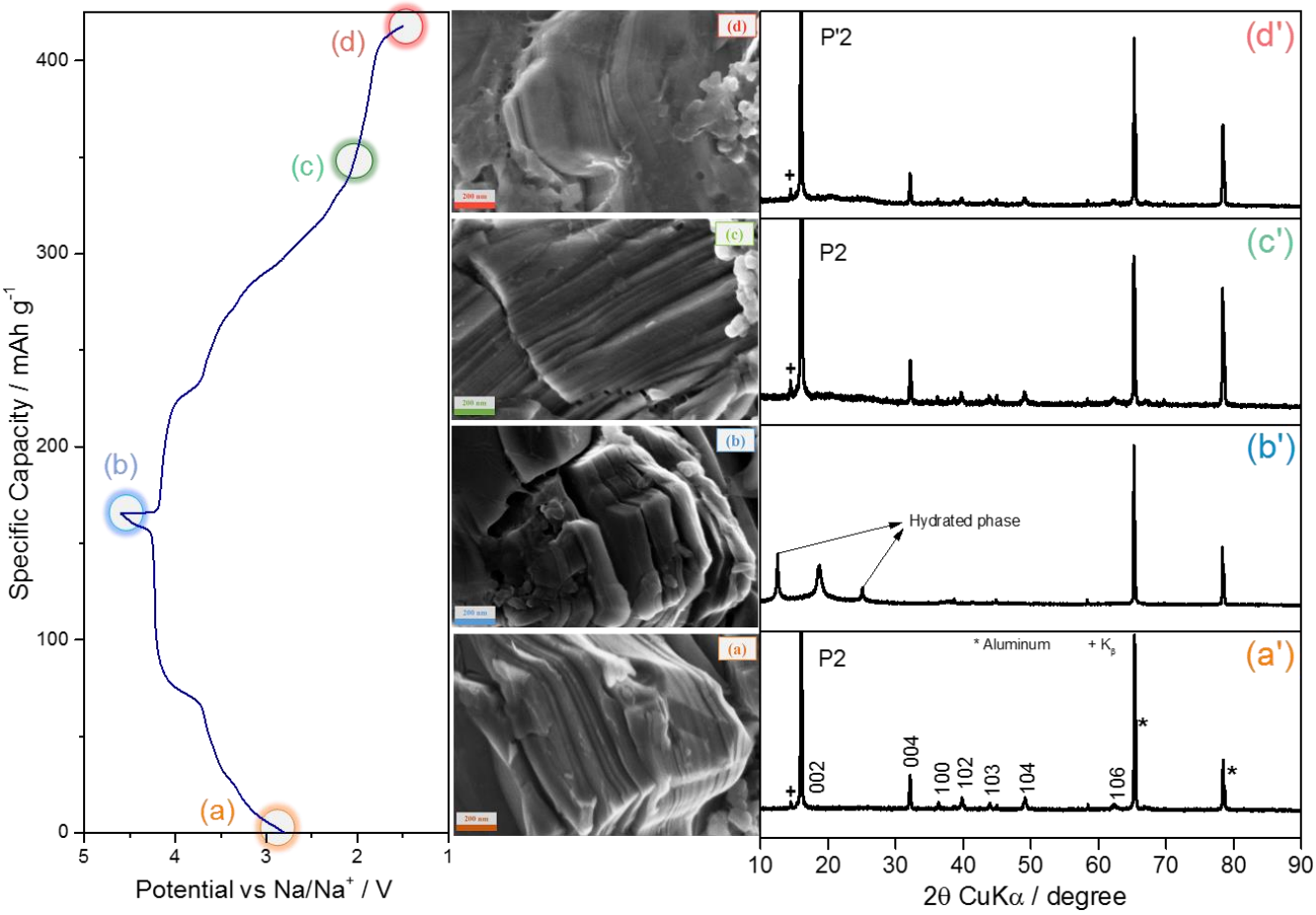
Specific Capacity / mAh g-1
Potential vs Na/Na+ / V
(a)
(b)
(c)
(d)
(a')
(b')
(c')
(d')
P2
P'2
Hydrated phase
* Aluminum
+ Kβ
002
004
100
102
103
104
106
2θ CuKα / degree

Figure 5

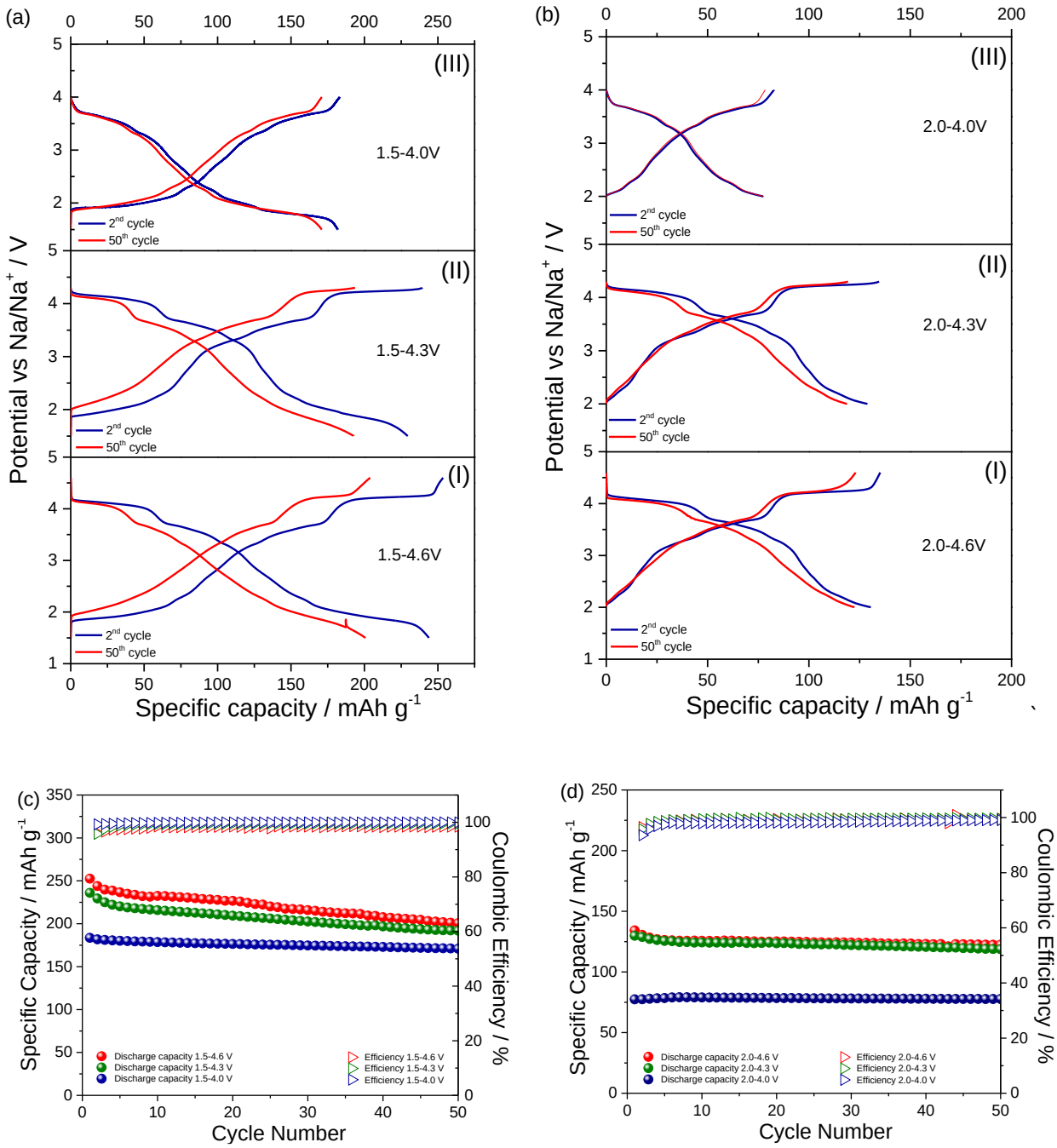
(a)
(III)
1.5-4.0V
(II)
1.5-4.3V
(I)
1.5-4.6V
2nd cycle
50th cycle
Potential vs Na/Na+ / V
Specific capacity / mAh g-1
(b)
(III)
2.0-4.0V
(II)
2.0-4.3V
(I)
2.0-4.6V
(c)
Discharge capacity 1.5-4.6 V
Discharge capacity 1.5-4.3 V
Discharge capacity 1.5-4.0 V
Efficiency 1.5-4.6 V
Efficiency 1.5-4.3 V
Efficiency 1.5-4.0 V
Specific Capacity / mAh g-1
Coulombic Efficiency / %
Cycle Number
(d)
Discharge capacity 2.0-4.6 V
Discharge capacity 2.0-4.3 V
Discharge capacity 2.0-4.0 V
Efficiency 2.0-4.6 V
Efficiency 2.0-4.3 V
Efficiency 2.0-4.0 V

Figure 6

Voltage range / V vs Na^+/Na	Discharge capacity at 1st cycle / mAh g^{-1}	Discharge capacity at 50th cycle / mAh g^{-1}	Capacity retention at 50th cycle / %	Coulombic Efficiency at 50th cycle / %	Average working voltage / V vs Na/Na^+				Sodiation Voltage efficiency after 50 cycle / %
					2nd cycle		50th cycle		
					Sodiation	De-sodiation	Sodiation	De-sodiation	
1.5-4.6	252.5	200.6	79.5	98.38	2.93	3.14	2.86	3.23	97.6
1.5-4.3	231.6	191.8	82.8	99.45	3.00	3.21	2.91	3.28	97.0
1.5-4.0	183.6	170.9	93.1	99.97	2.56	2.7	2.55	2.73	100
2.0-4.6	134.2	122.5	91.2	99.56	3.97	3.59	3.83	3.55	96.4
2.0-4.3	130	118.8	91.5	99.55	3.71	3.57	3.60	3.53	97.0
2.0-4.0	77.4	77.5	100	99.07	2.95	3.10	2.94	3.09	100

Table 2

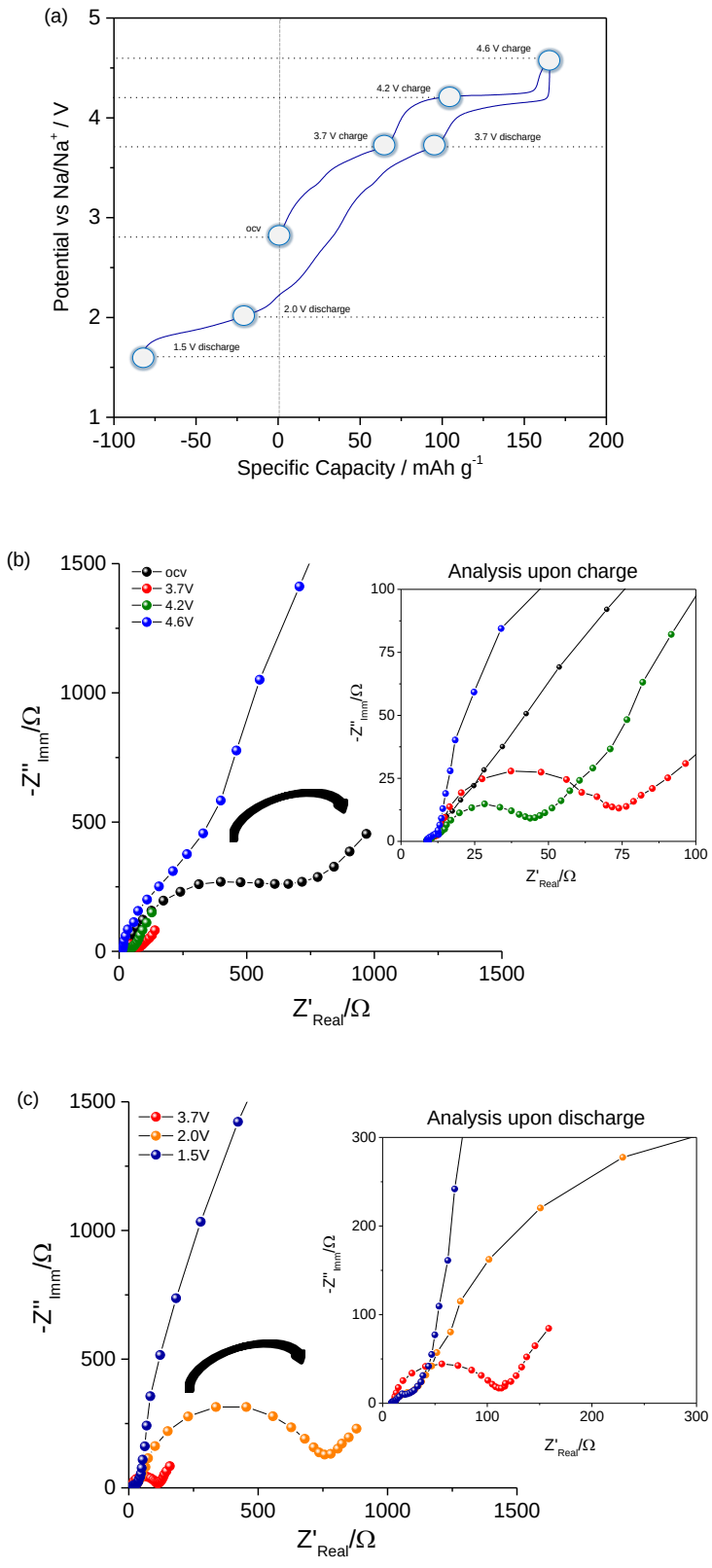
(a)
Potential vs Na/Na+ / V
Specific Capacity / mAh g-1
4.6 V charge
4.2 V charge
3.7 V charge
3.7 V discharge
ocv
2.0 V discharge
1.5 V discharge
(b)
ocv
3.7V
4.2V
4.6V
-Z''Imm/Ω
Z'Real/Ω
Analysis upon charge
(c)
3.7V
2.0V
1.5V
Analysis upon discharge

Figure 7